Article

The origin of interplanetary switchbacks in reconnection at chromospheric network boundaries

Check for updates

Chuanpeng Hou [1], Jiansen He [1] ✉, Die Duan[1], Ziqi Wu[1], Yajie Chen [2], Daniel Verscharen [3] ✉, Alexis P. Rouillard [4] ✉, Huichao Li [5], Liping Yang[6] & Stuart D. Bale[7,8]

There is renewed interest in heliospheric physics following the recent exploration of the pristine solar wind by the Parker Solar Probe. Magnetic switchback structures are frequently observed in the inner heliosphere, but there are open questions about their origin. Many researchers are investigating the statistical properties of switchbacks and their relationships with wave modes, stream types and solar activity, but the sources of switchbacks remain elusive. Here we report that interplanetary switchbacks originate from magnetic reconnection on the Sun that occurs at chromospheric network boundaries and launch solar jet flows. We link in situ interplanetary measurements and remote-sensing solar observations to establish a connection between interplanetary switchbacks and their solar source region, featuring solar jets, chromospheric network boundaries and photospheric magnetic field evolution. Our findings suggest that joint observations of switchbacks and solar jets provide a better estimate of the contribution of magnetic reconnection to coronal heating and solar wind acceleration.

Since its successful launch, the Parker Solar Probe (PSP)[1] has approached closer to the Sun than other probes, and its in situ measurements have filled a gap in our understanding of the conditions of young solar wind and interplanetary magnetic fields at heliocentric distances below 0.3 au. Frequent deflections, and even inversions, of the interplanetary magnetic field are a notable finding of PSP[2,3]. The pitch angle distribution of strahl electrons remained the same as PSP passed through the reversal region boundary[4], suggesting that the reversal is not due to a current sheet or closed magnetic loop, but to the bending of magnetic field lines. The geometry of these inversions thus led to these structures being called magnetic switchbacks. Before the launch of PSP, other

spacecraft had detected such switchback structures at different helio-centric distances—for example, Helios between 0.3 au and 1 au (ref. 5), ACE near Earth[6] and Ulysses beyond 1 au (ref. 7). However, the significant difference is the higher frequency of switchbacks observed by PSP and the more prominent features of the plasma in these switchbacks, such as their increased radial velocity[3,8] and higher temperature[8]. The measurement of switchbacks and the study of their formation mechanism provide new opportunities to resolve several key issues in solar physics, such as the heating of the corona[9] and the acceleration of the solar wind[10].

The recent literature proposes primarily three classes of switch-back generation mechanism, and each process is able to explain some

[1]School of Earth and Space Sciences, Peking University, Beijing, China. [2]Max-Planck Institute for Solar System Research, Göttingen, Germany. [3]Mullard Space Science Laboratory, University College London, Dorking, UK. [4]IRAP, Université Toulouse III-Paul Sabatier, CNRS, CNES, Toulouse, France. [5]Institute of Space Science and Applied Technology, Harbin Institute of Technology, Shenzhen, China. [6]State Key Laboratory of Space Weather, National Space Science Center, Chinese Academy of Sciences, Beijing, China. [7]Physics Department, University of California, Berkeley, Berkeley, CA, USA. [8]Space Sciences Laboratory, University of California, Berkeley, Berkeley, CA, USA. ✉e-mail: jshept@pku.edu.cn; d.verscharen@ucl.ac.uk; arouillard@irap.omp.eu
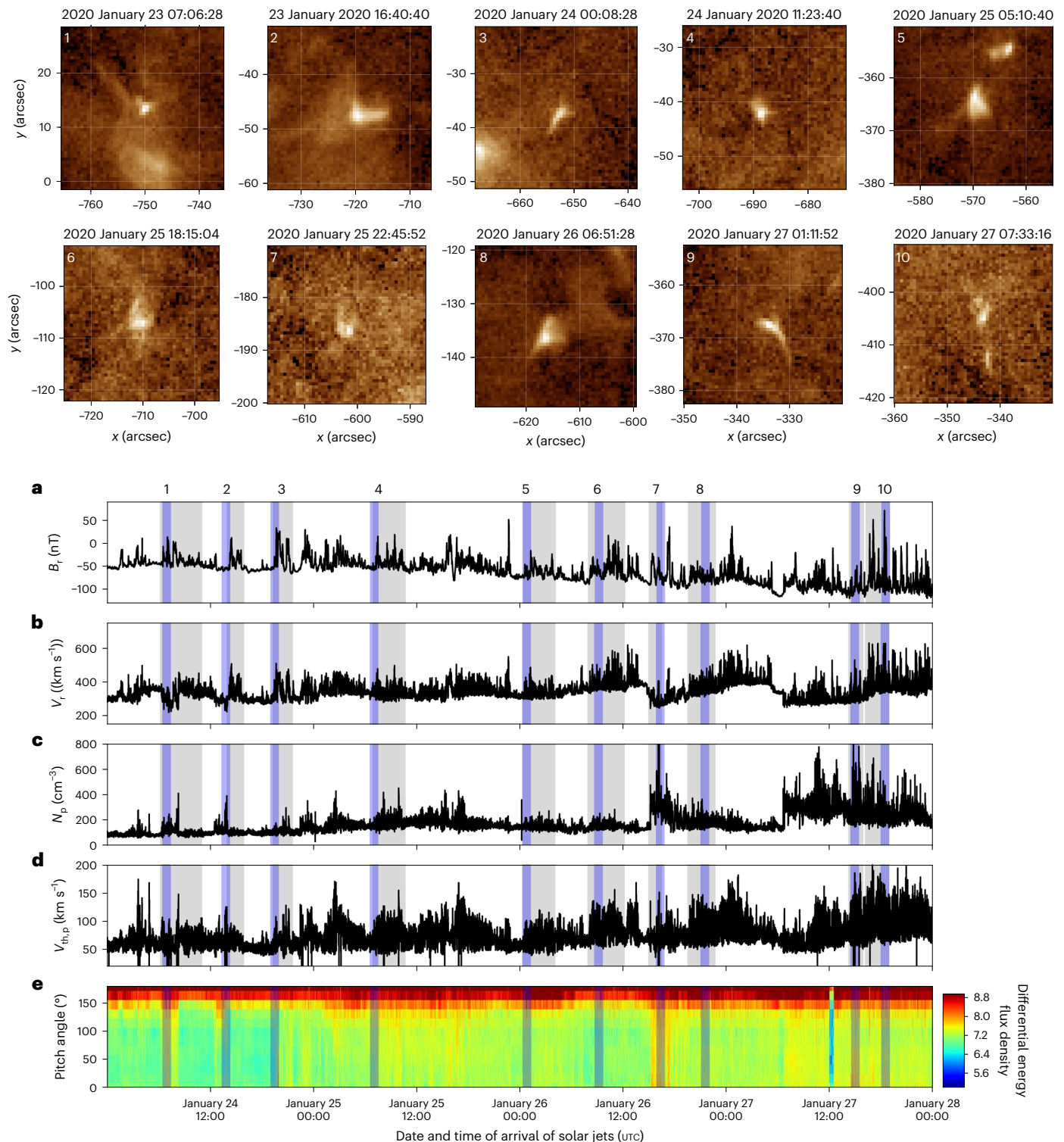
Fig. 1 | Correspondence between solar jet events and switchback clusters.
The numbers 1–10 represent the ten jet events observed by AIA at 193 Å that
were launched from the footpoints of magnetic field lines connecting to the
switchback clusters observed by PSP. The dates and times of the events are listed
above the images. **a**, The radial magnetic field component (B_r) measured by PSP's
flux-gate magnetometer. **b**, The radial solar wind velocity (V_r) measured by PSP/
SPC. **c**, The number density of protons (N_p) measured by PSP/SPC. **d**, The proton
thermal velocity ($V_{th,p}$) measured by PSP/SPC. **e**, The pitch angle distribution
of electrons in an energy range of ~314–786 eV measured by the Solar Probe
Analyzers-Electrons aboard PSP. The blue shaded bars mark the times when the
associated disturbances arrive at PSP's position with an uncertainty of 1 h. The
grey shaded areas in **a**–**d** represent the time intervals of switchback clusters.

of the observational features of switchbacks. The first major category
is the steepening of wave modes that propagate outwards from the
solar atmosphere[11–13]. This theory accounts for different excitation
processes of wave modes, such as Alfvén waves[13] generated by magnetic

reconnection in the solar atmosphere and Alfvén waves[11] generated
by the shuffling of the footpoints of magnetic field lines due to pho-
tospheric convection. In simulations of interchange magnetic recon-
nection with guide-field discontinuity[13], the resulting magnetic fields,

velocities, densities and temperatures are close to those of switchbacks observed by PSP. Alfvén wave excitation thus potentially plays an important role in providing the seed of switchback structures. The propagation of large-amplitude Alfvén waves in the expanding solar wind[11] and the turbulence[14] driven by Alfvén waves are potentially responsible for the development of switchbacks. The second category of proposed switchback production mechanisms refers to more rigid magnetic structures carried into interplanetary space by the solar wind, such as kinked magnetic field lines[12] and magnetic flux ropes[15]. One numerical simulation suggested that the kinked magnetic field lines largely maintain their morphology to the orbital distance of PSP during outward propagation[16]. The third category considers the perturbation of magnetic field lines due to stream interactions. For example, the footpoint of a magnetic field line rapidly transfers from a low-speed flow zone to a high-speed flow zone (such as a coronal hole), forming a super-Parker spiral that produces a switchback beyond the Alfvén critical point[17]. In addition, in magnetohydrodynamic (MHD) simulations, nonlinear shear-driven turbulence also produces switchback-like fluctuations under certain circumstances[18]. All of these scenarios and theories are reasonable but further observational evidence is needed to obtain a definitive conclusion.

PSP's observations during several encounters show that switchbacks tend to appear in clusters and that the spatial distribution of switchback clusters is comparable to the typical size of a supergranulation[19]. These findings suggest that switchback clusters originate at, or are modulated by, supergranulation cell boundaries[19], where the magnetic field lines usually protrude from the photosphere into the corona[20]. The magnetic reconnection between the open and surrounding closed magnetic field lines naturally becomes the most likely source of switchbacks in this scenario. Numerous models for the excitation of solar jets have been proposed based on both remote sensing and simulations[21]. These models, including the emerging-reconnection model[22], embedded-bipole model[23] and breakout jet model[24], all identify magnetic reconnection as the central process responsible for jet initiation. The distinctions among these models primarily concern the triggering of magnetic reconnection. This can involve factors such as the emergence or cancellation of photospheric magnetic fields[25–27] or the shearing motion of magnetic loop footpoints[28]. A series of studies[29–31] revealed that small-scale solar jets excited by magnetic reconnection exhibit lifetimes similar to the duration of switchbacks in the solar wind. These observations led to the proposition that solar jets may serve as a source of switchbacks.

MHD simulations show that there is a heat flux conducting outwards along the magnetic field lines during interchange reconnection[13], in addition to magnetic flux ropes, fast/slow mode waves and Alfvén waves[32]. Recent work comparing Solar Terrestrial Relations Observatory (STEREO) and PSP observations revealed that switchback clusters are often measured jointly with significant changes in the local plasma density, especially when they form inside streamers[33]. Density fluctuations are common in the corona and could be produced during small eruptions and jets triggered near the surface of the Sun[34]. Based on these observations and simulations, we speculate that small solar jets and switchbacks may be two characteristics of the same physical process. We establish a causal link between solar jets and interplanetary switchbacks with a two-step ballistic backmapping method (described in full in the Methods). The Atmospheric Imaging Assembly (AIA) and Helioseismic and Magnetic Imager (HMI) aboard the Solar Dynamic Observatory (SDO)[35] provide multi-waveband extreme ultraviolet images and line-of-sight magnetic field measurements of the Sun with cadences of 12 s (AIA) and 45 s (HMI). The measurements taken by PSP's flux-gate magnetometer, Solar Probe Cup (SPC) and Solar Probe Analyzers-Electrons[4] provide data for magnetic fields, protons and electrons at cadences of 60 s, 0.44 s and 14 s, respectively. During the fourth solar encounter of PSP, the spacecraft was nearly aligned with the SDO spacecraft as viewed from the Sun, facilitating our synergistic study of the same solar wind stream and associated turbulence from both in situ measurements and remote-sensing observations.

Results

In PSP observations between 2020 January 24 and 2020 January 27, we found that the sudden changes in the radial magnetic component occurred in clusters (Fig. 1a), with the peak of the strahl electron pitch angle distribution remaining near 180° during the magnetic field reversal (Fig. 1e). Consistently with previous work, we thus confirmed that PSP observed several clusters of switchbacks. These switchbacks were accompanied by increased radial velocity (Fig. 1b) and increased temperature (Fig. 1d) of the solar wind protons, as well as non-significant changes in density (Fig. 1c). By visually identifying the projection points of switchbacks on the solar photosphere and AIA 193 Å images (Methods), we found a total of ten small solar jets (Fig. 1; see Supplementary Videos 1–10). These jets were all accompanied by bright Y-shaped structures at the base and two magnetic fragments of opposite polarities (Supplementary Videos 1–10), which are typical features of magnetic field reconnection[36]. We highlight the moment when the plasma/structure originating from the solar jets arrived at PSP with blue shading in Fig. 1. We found that the excitation of each jet corresponded to a cluster of switchback structures.

Taking jet 2 in Fig. 1 as an example, we applied the linear force-free field extrapolation method[37] to the line-of-sight components of the photospheric magnetic field observed by HMI (Fig. 2c) to obtain a three-dimensional magnetic field distribution in the vicinity of the jet (Fig. 2b). The topology of the magnetic field lines matched the magnetic configuration expected to trigger magnetic reconnection between open and closed magnetic field lines[13]. In addition, a higher ion temperature was measured in the PSP observations during Alfvénic magnetic field reversals than in the surrounding background solar wind (Fig. 1d). These measurements are consistent with MHD simulation results for Alfvénic pluses launched from interchange reconnection sites, from which the compressional wave and heat flux propagate outwards along the magnetic field lines[13].

Next, we analysed the solar chromospheric images taken by the He II 304 Å passband of SDO/AIA and plotted the distribution of He 304 Å radiation in the region related to jet 2 in Fig. 2a. We introduced the method of image segmentation with watershed algorithm and successfully identified and outlined the chromospheric network boundaries (red curves in Fig. 2a). In the vicinity of jet 2, we performed a linear force-free field extrapolation based on the observation of the photospheric magnetogram to obtain the open magnetic flux tube of the corresponding funnel-like structure (marked in Fig. 2a with yellow grid lines). The funnel-shaped root of the open magnetic structure was near the boundary of the chromospheric network. In fact, the topology and polarity of the magnetic lines at the root of this structure look like a typical null-point reconnection configuration (Fig. 2b): it is divided into three divergent strands, which land in three magnetic fields of different polarities on the photosphere. Such a distribution of topological patterns is typical for magnetic reconnection[13].

The results of these analyses indicated that the jets associated with the origin of switchbacks were driven by magnetic reconnection occurring at the boundary of the chromospheric network. The multi-passband AIA images show the features of solar atmosphere materials with different temperatures. For example, imaging of the 304 Å passband usually corresponds to materials with a temperature of 0.5 million kelvin, whereas other passbands such as 171 Å, 193 Å, 211 Å and 335 Å successively image the higher-temperature atmosphere. All of these Y-shaped structures of jets appear in the 304 Å passband, but they are blurred in the 335 Å passband (Fig. 2c). Emission measure loci show that the brightness may be contributed mainly by materials with a temperature of 0.28 million kelvin (Supplementary Fig. 1), which is the typical temperature of the transition region. The excitation region
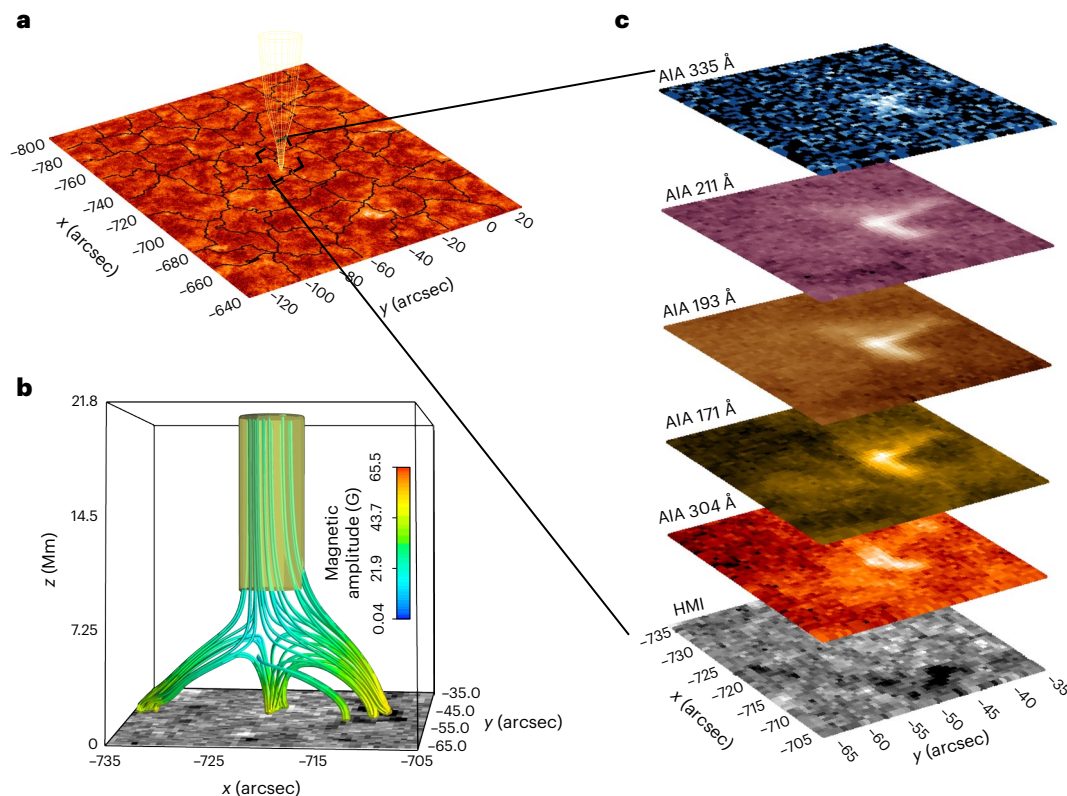
Fig. 2 | One solar jet event on 2020 January 23. a, Position of the jet on the AIA 304 Å image. The magnetic flux tube (in yellow) shows the position of the jet. The black curves superposed on the background image represent the boundaries of the chromospheric network. The white rectangle marks the areas shown in **b** and **c. b**, The magnetic field geometry obtained by linear force-free field extrapolation in the vicinity of the jet. The colour along the magnetic field lines shows the amplitude of the local magnetic field from low (blue) to high (red).

The bottom ends of the magnetic field lines connect to the HMI magnetogram, with white and black representing positive and negative magnetic polarity. The yellow tube represents the corresponding magnetic flux tube. **c**, HMI magnetogram and multi-waveband AIA images from 2020 January 23 16:41:41 arranged by the peak temperatures of the response functions. The HMI magnetogram is the same as in **b**. The bright areas in AIA images show the morphology of the jet.

of jets could therefore be located at the transition region or slightly higher corona.

The time cadence of 45 s of the solar magnetograms recorded by HMI enabled us to estimate the change in magnetic flux that may be responsible for magnetic reconnection. We found that seven out of the ten cases experienced a decrease in magnetic flux (magnetic cancellation), whereas three jet events were accompanied by a slightly ambiguous change in the magnetic flux, which we could only interpret as a tendency towards magnetic flux emergence. Using the tangential velocity component of the solar wind and the radial magnetic field component measured by PSP, we obtained the direction-switched magnetic flux in the switchback clusters (Fig. 3) under the assumption that PSP traversed flux tubes with circular cross-sections along the diameter direction. We found a clear positive correlation (with a correlation coefficient of 0.81) between the interplanetary switchback-related magnetic flux change and two times the jet-associated magnetic flux change. The positive correlation had a linear slope of 0.74, which is less than 1, probably due to the assumption of a circular flux tube that would overestimate the area of the in situ magnetic flux tube. This correlated phenomenon indicates a physically intrinsic relationship between switchbacks, solar jets and magnetic reconnection.

We marked the locations of the ten jets on the solar surface (Fig. 4a,b). They were distributed mainly in the southern hemisphere and were not located on the boundaries of the same network structure, but on the boundaries of different network structures that were not very far apart. The bending and expansion of the magnetic flux tubes associated with the jets led to a neighbouring distribution of switchback clusters after extending into interplanetary space, although their

roots were not co-located (Fig. 4c). The solar wind states (for example, flow speed, temperature) in these ten different open magnetic flux tubes were also dissimilar. Some of the intervals showed higher flow speeds and temperatures (for example, the magnetic flux tubes corresponding to jets 6 and 10). In contrast, others had lower flow speeds and temperatures (for example, the magnetic flux tubes corresponding to jets 1 and 7). When PSP successfully crossed the magnetic flux tubes with high- and low-speed solar wind, it detected changes in the solar wind flow velocity and temperature. These changes can be fast, forming quasi-discontinuous changes (for example, crossing from jet 6 to jet 7; Fig. 1b,d). In addition to the different background solar wind states, all observed magnetic flux tubes were accompanied by intermittent speed spikes and magnetic switchbacks. These spikes and switchbacks had strong Alfvénicity in their associated in situ measurements.

Discussion

Our study shows that interplanetary switchbacks, solar jets and magnetic reconnection are correlated. Solar jets and interplanetary switchbacks are probably two observable phenomena caused by the same magnetic reconnection process. Combined with the correlation between jets and switchbacks, our findings suggest that the switchbacks originate from a magnetic reconnection in the transition region or the low corona and at the boundaries of the chromospheric network. Parameters such as the occurrence rate of switchbacks and the amount of magnetic flux associated with the deformation of magnetic field lines within switchbacks will be helpful in diagnosing the occurrence rate and duration of coronal magnetic reconnection, and thus quantifying the transport of energy and mass into interplanetary space by the turbulent solar wind.
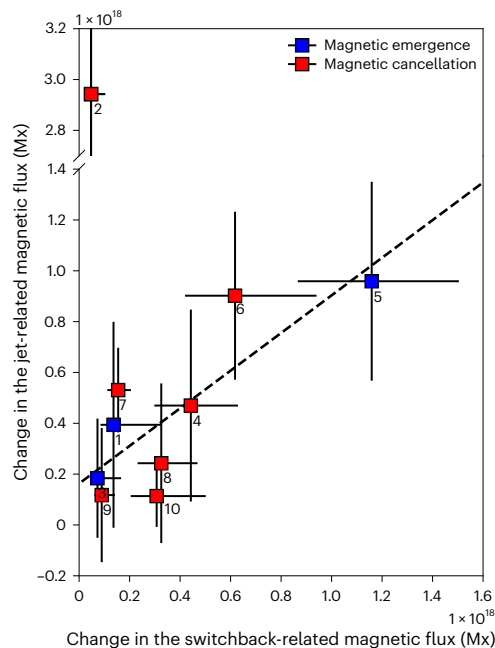
Fig. 3 | The change in magnetic flux related to solar jets and switchback clusters. The magnetic emergence is not clearly visible in Supplementary Videos 1–10. The magnetic flux change of jet 2 in units of Maxwell (Mx) deviates significantly from the others. After excluding this data point, the linear fitting yields a slope of 0.74 for the dashed line and a correlation coefficient of 0.81. The y-axis values and error bars of the data points are the mean ± s.e.m. and x-axis values and error bars are calculated from the in situ measurement and its uncertainty as described in the Methods. The numbers of data points used to calculate the change in the photospheric magnetic flux for jets 1–10 are 19, 27, 24, 21, 25, 16, 17, 22, 20 and 17, respectively.

There are a few switchback clusters shown in Fig. 1 without corresponding solar jet events, such as the switchback clusters on 2020 January 24 at 22:00 to ~07:00 on 2020 January 25, 2020 January 25 at 12:00 to ~00:00 on 2020 January 26 and 2020 January 27 at 00:00 to ~14:00. We suggest two possible reasons for the absence of observable solar jet events: (1) the jet flow may be along the line of sight, which results in a lack of elongated jet structures or (2) these jets may be inconspicuous jets, such as those defined in ref. 38. Sterling et al.[38] found that some jets appear only as a bright base in soft X-ray images, but exhibit strong jet features in Doppler velocity fields. Although on-disk jetlets are not easy to observe, they have been the focus of attention in the academic community, with efforts made to observe and identify them. Recently, on-disk jetlets have been observed by telescopes such as AIA, Interface Region Imaging Spectrograph and High Resolution Coronal Imager at the edges of magnetic network boundaries[39–41]. In Solar Orbiter/Extreme Ultraviolet Imager images, some small-scale brightening events (named campfires) have been reported. Joint observations from SDO/AIA and Solar Orbiter/Extreme Ultraviolet Imager at extreme UV and Lyman α wavelengths suggest that these campfires are rooted at network boundaries in the heights of the transition region or corona[42]. Most campfires exhibit features of jets and are accompanied by the cancellation of opposite-polarity magnetic fields[43]. Besides campfires, brightening events associated with small-scale loop complexes also feature magnetic reconnection and eruptive activity[44,45]. It is therefore appropriate to choose brightening events as a proxy of jets. In Supplementary Fig. 2 we show the time series of brightening numbers and the time series of switchback measurements from 15:00 on 2020 January 23 to 08:00 on 2020 January 24. The positive correlation indicates that brightenings/jets are potential sources of switchbacks. We calculated the radiation intensity in the AIA 193 Å images corresponding to the footpoint region of

switchbacks over a longer time interval (from 2020 January 21 to 2020 January 29). The probability distribution of AIA 193 Å intensity in the footpoint region varied with time, and the intermittent changes in the radiation distribution associated with brightenings were similar to the intermittent occurrence of interplanetary switchback clusters (Supplementary Fig. 3). We expect relatively low eruptive activity in the solar source region of the quiet solar wind, as shown in Supplementary Fig. 4. A detailed discussion of the correspondence between solar jets and switchbacks is included in the Supplementary Information.

While our results clearly show signatures that are consistent with the model of interchange reconnection as the origin of switchbacks, this work cannot rule out additional and alternative scenarios, such as Alfvén waves caused by the reshuffling of magnetic line footpoints in the photosphere due to the random collision of converging convection plasma patches at network boundaries[46]. Alfvén waves launched from the photosphere can experience amplitude amplification and nonlinear steepening in expanding structured magnetic flux tubes with gravity stratification[47], which are usually rooted at the network boundaries. The lower solar atmosphere, with sharp transitions in physical quantities, serves as a wave filter by blocking/reflecting a large proportion of those outward waves—only 5% escape across the solar transition region[48], especially those at a longer wavelengths[49]. Therefore, the possibility that Alfvén waves originate from the photosphere and directly evolve into coronal or interplanetary Alfvénic switchbacks is greatly reduced. However, we cannot rule out the role of filtered outward waves. Outward waves with a small, but finite, amplitude at the coronal base could potentially contribute to the formation of switchbacks in a turbulent environment[11,14].

A series of works[29–31] proposed coronal jets, jetlets and even smaller jets as the sources of switchbacks and estimated the duration of switchbacks considering the radial profile of the Alfvén speeds. According to these studies, the duration of switchbacks originating from coronal jets with a typical lifetime of 10 min is about 25 min. However, in our work, the switchback clusters lasted much longer than the lifetimes of the jets, which we interpreted as follows. A statistical study[50] showed that in the heliocentric range between 20 surface radii (R_s) and 100 R_s, the radial size of switchbacks increases as the square of the radial distance (~R^2). Hence, their expansion increases the duration compared with the solar surface counterparts. Another possible reason is that the jets, during their outward propagation, disturb the ambient field and excite additional fluctuations[51]. These additional fluctuations may also steepen to magnetic kinks and switchbacks. Tian et al.[36] reported the prevalence of smaller jets rooting at network boundaries of the solar transition region and chromosphere. These smaller jets exhibited short lifetimes (~20–80 s), widths of less than 300 km (smaller than the resolution of AIA and HMI and barely detectable by AIA and HMI), brightenings and sometimes Y-shape footpoints (resulting from magnetic reconnection). They also displayed transverse fluctuations that probably correspond to outward Alfvén waves. Hence, it is possible that the solar jets in our work may be accompanied by these abundant, but invisible, smaller jets or brightenings shown by Tian et al.[36], thus explaining the long duration of switchback clusters compared with the durations of single large solar jets. There is indeed a positive correlation between the occurrence of intense reversals of the radial component of the magnetic field and the number of coronal brightenings (Supplementary Fig. 2). We consider the study of the intricate relationships between the phenomena affecting the duration of switchbacks worthy of future investigation. Our work reveals the state of switchbacks in interplanetary space and their origin on the Sun. However, we did not address the propagation of switchbacks from their place of origin into space. Therefore, in future work it will be important to identify and track the propagating evolution of switchback structures from remote-sensing imaging of the dynamic corona into the inner heliosphere. Telloni et al.[52] recently made an insightful attempt to identify one possible event, the estimated propagation speed of which was slower than the local Alfvén
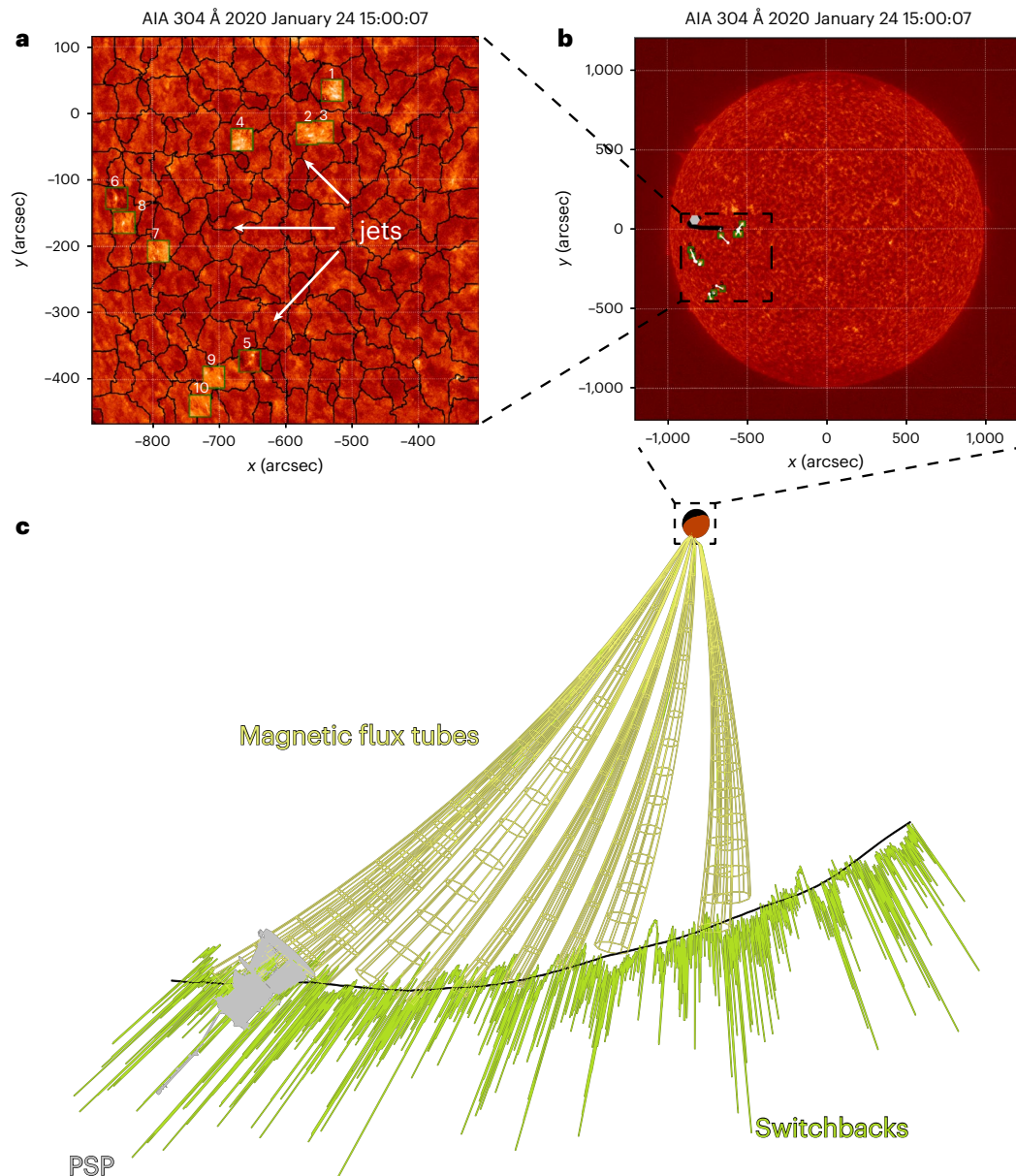
Fig. 4 | The relationship between solar jets and switchback clusters.
a, Distribution of solar jets (green boxes labelled with jet numbers) in the field of
view of AIA 304 Å. The black lines mark the chromospheric network boundaries.
b, The full solar disk AIA 304 Å image. The grey hexagon represents PSP's
projection point at the time of the image, and the black line shows the trajectory
of PSP on the source surface. The white points connected to each jet represent
the footpoints of magnetic field lines on the solar photosphere. Please note that
we use a solar chromosphere image taken at 15:00 on 2020 January 24 at 304 Å

wavelength as the background. We then overlaid the small patch regions of jet
events associated with PSP-observed switchbacks based on their respective
Carrington longitude and latitude ranges onto the background image. **c**, The
magnetic flux tubes connecting the solar surface and switchback clusters. The
yellow tubes represent magnetic flux tubes and the black line shows the orbit
of PSP. The green disturbance represents the radial magnetic component and
shows the distribution of switchback clusters along PSP's orbit.

wave. Multi-point observations of the Sun and inner heliosphere (with
PSP, Solar Orbiter, SDO, Solar Terrestrial Relations Observatory and
so on) will create favourable observation conditions to uncover the
origin and formation of switchbacks. For example, the joint observa-
tion of the same switchback structure by two spacecraft (one taking
in situ measurements and the other taking images remotely) will help
reveal the structure of the switchback, including its kinematics and
dynamics. In addition, advanced numerical simulations are also a
powerful means to resolve this critical problem in the research field of
solar and heliospheric physics. Based on solar surface observations as
time-varying, data-driven inner boundary conditions, (quasi-) global
multi-fluid MHD numerical simulation are expected to be capable of

investigating the causal chain formed by the origin of switchbacks at
the boundary of the chromosphere network and their propagation into
the corona and inner heliosphere.

Methods
Two-step ballistic backmapping method
By integrating the in situ measurements and remote-sensing obser-
vations, we established a causal link between interplanetary switch-
backs and small solar jets, thereby determining the source region and
generation mechanism of switchbacks. We used a two-step ballistic
backmapping method[2,53] to identify the magnetic field lines connect-
ing the solar surface and PSP. We then used the radial speed of the

switchbacks and PSP's orbital positions to predict the origin time of the disturbance counterpart on the Sun corresponding to the switchback in interplanetary space.

Based on the potential field source surface (PFSS) model[54], we used PFSSPy[55], a publicly available Python package, to calculate the magnetic field between the photosphere and the source surface. The PFSS model solves the Laplace equation for the potential magnetic field with the observed photospheric synoptic map as the lower boundary condition and the presumed radial alignment of magnetic fields on the source surface as the upper boundary condition. In combination with the magnetic field distribution, PFSSPy's built-in field line tracer provided us with information about the magnetic field strength and photospheric footpoint of a magnetic line connecting any given point below and on the source surface. We compared PSP's flux-gate magnetometer[56] measurements, the thermodynamic MHD model from Predictive Science Inc. (PSI) and the PFSS modelling results at different source surface radii (1.2 R_s, 1.5 R_s, 2.0 R_s and 2.5 R_s) (Supplementary Fig. 5). Source surface radii of 2.0 R_s and 2.5 R_s provided better agreement with the observations. During solar minimum, a lower source surface radius opens more field lines from low-latitude coronal holes and improves the consistency of the model extrapolations with observations[2,57]. Given that our analysis was performed during a solar minimum period, we used the lower 2.0 R_s instead of the standard 2.5 R_s. The extrapolated magnetic field calculated from 2.0 R_s also matched the structural features of coronal holes and streamers shown in AIA 193 Å and the CoOronal Solar Magnetism Observatory (COSMO) K-coronagraph white-light corona images (Supplementary Fig. 6). Moses et al.[58] identified a correlation between helium abundance (represented by the ratio of the helium density to the proton density) and solar latitude during solar minimum. The plasma shows significantly lower helium abundances ($N_{He}/N_p < 2\%$) near the equatorial region at low latitudes, whereas the abundance of helium ions in the high-latitude coronal regions is higher than 10%. Motivated by this work, we calculated the helium abundance measured by PSP from 2020 January 20 to 2020 January 31. The probability density distribution of the helium abundance is shown in Supplementary Fig. 7. Both the median and mean of the helium abundance are less than 1%, consistent with the low helium abundance in low-latitude regions shown by Moses et al.[58]. On the other hand, Kasper et al.[59,60] found that the in situ slow solar wind has a lower helium abundance at solar minimum, even lower than 1%. Hence, the solar wind measured by PSP in our work could be classified as slow solar wind, which usually originates from low-latitude solar areas at solar minimum[59,61]. According to the above explanation, a source surface radius of 2.0 R_s used here, which gives footpoints concentrated at lower latitudes than 2.5 R_s, seems more appropriate. We used the hourly updated synoptic map from Global Oscillation Network Group (GONG) of National Solar Observatory (NSO) for the photospheric synoptic map.

We considered the magnetic field outside the source surface to be frozen with the quasi-radially flowing solar wind. The solar rotation causes the interplanetary magnetic field lines to form the Parker spiral pattern[62]. Assuming that the solar wind travels outwards at a constant speed, by combining the orbital coordinates of PSP, we calculated the magnetic field lines connecting the source surface to the position of PSP. For this backmapping, we used the solar wind radial speed measured by PSP/SPC[63]. In the second step, the magnetic field line connecting PSP and the source surface was traced back to the photosphere using the 3D magnetic field calculated by the PFSS model. Combining the PFSS model and the Parker spiral pattern, we identified the magnetic field line connecting the photosphere to PSP. After considering the influence of the Sun's rotation and solar wind acceleration, the position error in the longitude of the magnetic field line footpoint on the photosphere obtained by the two-step ballistic backmapping method was usually less than 10° (ref. 2).

We compared the positions of the footpoints of the magnetic field lines given by the coronal thermodynamic 3D MHD simulation and the two-step ballistic backmapping method. We found that the longitudes of footpoints given by the two methods were similar, with the MHD simulation yielding significantly higher latitudes for the footpoints. As shown in Supplementary Fig. 5, the PFSS model was able to provide better magnetic extrapolations than the MHD model during the time interval in our work. The MHD simulation used one synoptic magnetogram for each Carrington rotation, and the two-step backmapping method used an hourly updated synoptic magnetogram. Therefore, we speculate that the solar magnetic field's evolution led to the latitude differences of footpoints obtained from the MHD simulation and the two-step ballistic backmapping method.

The propagation speed of a jet-like Alfvénic pulse in the solar inertial reference frame can be viewed as the sum of the solar wind flow velocity and the propagation speed of the pulse in the solar wind flow reference frame. The propagation speed of the Alfvén pulse in the solar wind flow reference system can be approximated as the local Alfvén speed[7,12,14,64]. Thus, the propagation time of an Alfvénic pulse depends on the radial profile of the solar wind flow velocity and the Alfvén speed between its solar source region and the location of PSP. Unfortunately, due to the limitations of local measurements from a single satellite, obtaining precise radial profiles of these velocities is challenging. As a result, we had to calculate the propagation time based on the assumption that the radial propagation speed of the Alfvénic pulses in the solar inertial reference frame remained constant, which is the sum of the solar wind flow velocity (V_{sw}) and the local Alfvén speed (V_A).

To validate the above assumption, we used PSI's coronal simulation data for solar wind velocity and Alfvén speed. Initially, we computed the outward propagation time as a function of distance based on the sum of the solar wind flow velocity and the Alfvén speed provided by PSI's simulation data. We adjusted the Alfvén speed provided by PSI by a factor of 4.7, which was calculated from the average measured and simulated radial magnetic field shown in Supplementary Fig. 5 ($\frac{<B_{r,psp}>_t}{<B_{r,PSI}>_t} \approx 4.7$). The adjusted Alfvén speed reached a maximum of approximately 1,000 km s^{-1}. With this adjustment, the Alfvén radius was located at a distance greater than 15 R_s, which was consistent with the results obtained by Kasper et al.[65]. We then calculated the propagation time as a function of propagation distance, assuming that the Alfvén pulse maintained a constant speed in the solar inertial reference frame (comprising the solar wind flow speed and the local Alfvén speed). We compared the disparity in propagation times resulting from these two calculation methods (Supplementary Fig. 8). The findings indicate that as the heliocentric distance increases, the distinction between these methods diminishes, converging to just a 1 h gap at a 10 h propagation time. This difference was noticeably smaller than the duration of the switchback clusters, as illustrated in Supplementary Fig. 8. Consequently, the minor relative deviations did not alter the conclusion that a temporal correlation exists between the jets/jetlets and switchback clusters. In our study, it is worth noting that PSP was situated beyond 30 R_s, which made the calculation of propagation times based on the assumption of constant propagation speed an acceptable approach.

Considering the propagation time deviations resulting from the constant velocity assumption, we show the arrival times of jets with shaded areas spanning time widths of 1 h in Fig. 1. Within an acceptable margin of error, the estimated jet propagation times to PSP aligned with the timing at which PSP detected the enhanced radial magnetic field fluctuations.

For the cases in our work, from the solar surface to the source surface, the field-aligned distance calculated from the PFSS model was greater than the radial distance by a margin of less than 0.3 R_s, indicating a minimal discrepancy. This discrepancy led to a deviation in propagation time of less than approximately 20 min when assuming an Alfvén speed of 150 km s^{-1} from the solar surface to the source surface. Taking into account a Parker spiral model of interplanetary magnetic field lines, the heliocentric distance of PSP (less than 0.23 au),

and the solar wind radial speed (500 km s^{-1}), we found that the angle between the field direction and the radial direction remained within 10°. As a result, the deviation in the propagation distance was less than 2%. Considering the points discussed above and acknowledging the limited information available on the actual propagation path and velocity of Alfvénic pulses, we proposed using the radial distance and solar wind velocity measured by PSP as an approximation to estimate the propagation time of Alfvén pulses.

Processing SDO images and converting coordinate systems
We obtained images of the regions of interest on the Sun (at first, regardless of the altitude difference) observed from the multi-waveband AIA[66] and HMI[67] telescopes using the Python package SunPy[68]. We also used SunPy to convert the coordinates of images among the heliographic inertial coordinate system, Carrington coordinate system and helioprojective-Cartesian coordinate system.

Determining the positions of the jets on the solar surface
After obtaining the photospheric footpoints of the magnetic lines connecting to PSP, we used SunPy to convert the footpoints' positions from Carrington coordinates to helioprojective-Cartesian coordinates. Given that the positions of the footpoints obtained by the two-step ballistic backmapping method usually had an error of about 10°, we visually identified the presence of jets within 100 arcsec of the footpoints and around the estimated launch time using the software JHelioviewer[69]. We list all of the jets we found around the footpoints in Fig. 1.

Calculating the unsigned magnetic flux changes
We used the magnetic fields measured by SDO/HMI with a time resolution of 45 s to obtain the change in the photospheric magnetic flux with time. At the bottom of each jet, we selected three areas (see the green boxes in Supplementary Videos 1–10 and Supplementary Table 1) to obtain time series of the unsigned magnetic flux located within the target area. The time interval for each jet is listed in Supplementary Table 1. Considering that the HMI 45 s data record the magnetic field only in the line-of-sight direction and the assumption that the photospheric magnetic field is usually in the radial direction[70], we corrected the total magnetic flux using $\Phi_1 = \Phi_0/\cos^2\theta$, where Φ_0 and Φ_1 are the magnetic fluxes before and after modification and θ is the angle between the jet's position and the centre of the solar disk.

We split the time series into two halves and calculated the mean and standard error of the magnetic flux separately. Then we obtained the change in the magnetic flux and the standard error during jet events. As we chose three areas for each jet to calculate the time series of the magnetic flux, the total change in the magnetic flux is the average over the three areas, as shown in Fig. 3. This approach of averaging over the three areas reduced the impact of imaging noise. An increase in the total magnetic flux after the excitation of the jet represented an event with magnetic emergence, and a decrease in the total magnetic flux represented an event with magnetic cancellation. Using jet 9 as an example, we provided three moments of the HMI magnetogram map and the AIA 193 Å map, which showed a decreasing unsigned magnetic flux during the jet's excitation, corresponding to a magnetic cancellation (Supplementary Fig. 9). We conducted separate statistical analyses on the three calculation regions to further elucidate the impact of the size of the calculation region. Specifically, we calculated the change in the photospheric magnetic flux ($\Delta\Phi_{\text{Sun}}$) for small, medium and large solar regions and examined its relationship with the change in the in situ measured magnetic flux ($\Delta\Phi_{\text{psp}}$) (Supplementary Fig. 10). The results revealed varying degrees of correlation between $\Delta\Phi_{\text{sun}}$ and $\Delta\Phi_{\text{psp}}$ for different calculation regions. It is worth noting that the correlation coefficients and R^2 indices indicated a stronger linear relationship for medium and large calculation regions compared with small regions. These results suggested that a larger calculation area may be necessary to fully capture the magnetic fields involved in the reconnection process, thereby minimizing the impact of area choice on statistical analyses.

There was a significant change in B_r for switchbacks relative to the background magnetic field. We used a sliding window of about 40 min to calculate the average value ($\langle B_r \rangle$) and standard deviation (σ_{B_r}) of B_r. If $\sigma_{B_r} > 10\%\langle B_r \rangle$, the data point was classified as a switchback; otherwise, it was considered to be part of the quiet solar wind. Hence, we quantitatively determined the intervals of each switchback cluster and calculated their corresponding in situ magnetic fluxes. We highlight the intervals with grey shaded areas in Fig. 1 and Supplementary Videos 1–10 for jets 1–10. The interval for each cluster is also listed in Supplementary Table 2. Assuming a circular cross-section of the magnetic flux tube associated with switchbacks, we obtained the cross-sectional diameter and area based on the tangential velocity of PSP relative to the solar wind. The PSP/SPC data provided the tangential velocity of the solar wind in the spacecraft reference frame and the upper and lower limits of the tangential velocity at the time of the switchback. Combined with the variation in B_r, we obtained the change in the radial magnetic flux and its upper and lower limits. We doubled the in situ magnetic flux to compare it with the unsigned photospheric magnetic flux. Our current methodology and single-point in situ measurements introduced bias in the flux statistics. Furthermore, the reconnection process occurring at the height of the transition region and corona had a smaller effect on the low-altitude photospheric magnetic field. Measurements of the magnetic field at multiple altitudes, such as the chromosphere, transition region and corona, are important to provide a more accurate picture of magnetic reconnection processes. We also look forward to the development of the solar magnetic imager with a higher signal sensitivity and spatial resolution.

Obtaining the 3D distribution of magnetic fields near the jets
The PFSS model provides the distribution of magnetic fields under the potential field assumption only, which is inaccurate when applied to a magnetic configuration with a current sheet, as is necessary for magnetic reconnection. Near the jets we employed a linear force-free field extrapolation program to the HMI magnetograms to obtain the magnetic field distribution. The extrapolation program is part of the SolarSoftWare package. We also used the MayaVi Python package[71] to visualize the extrapolated 3D magnetic field distribution.

Visualizing the magnetic flux tubes from the Sun to interplanetary space
Using the magnetic field magnitude obtained by PFSSPy, we calculated the expansion factor to determine the area of the flux tubes. The direction of the flux tube was the same as that of the magnetic field line serving as the tube axis. Beyond the source surface, we assumed that the flux tubes followed the Parker Spiral, and that the sectional area increased with the square of the radial distance.

Data availability
The data used in this work are publicly available. The PSP in situ measurement data are available at https://cdaweb.gsfc.nasa.gov/. AIA maps, HMI magnetograms and COSMO K-coronagraph images can be downloaded via SunPy at https://docs.sunpy.org/en/stable/index.html. GONG synoptic maps can be downloaded using the PFSSPy package at https://pfsspy.readthedocs.io/en/stable/index.html. The corona simulation data provided by PSI are available at https://www.predsci.com/mhdweb/home.php.

Code availability
The code packages used to read and process data are publicly available: SunPy is available at https://sunpy.org/; PFSSpy is available at https://pfsspy.readthedocs.io/en/stable/index.html; MayaVi is available at https://docs.enthought.com/mayavi/mayavi/index.html; and SolarSoftWare is available at https://www.lmsal.com/solarsoft/.

References

1. Fox, N. et al. The Solar Probe Plus mission: humanity's first visit to our star. *Space Sci. Rev.* **204**, 7–48 (2016).
2. Bale, S. et al. Highly structured slow solar wind emerging from an equatorial coronal hole. *Nature* **576**, 237–242 (2019).
3. Kasper, J. C. et al. Alfvénic velocity spikes and rotational flows in the near-Sun solar wind. *Nature* **576**, 228–231 (2019).
4. Whittlesey, P. L. et al. The solar probe analyzers-electrons on the Parker Solar Probe. *Astrophys. J. Suppl. Ser.* **246**, 74 (2020).
5. Horbury, T., Matteini, L. & Stansby, D. Short, large-amplitude speed enhancements in the near-Sun fast solar wind. *Mon. Not. R. Astron. Soc.* **478**, 1980–1986 (2018).
6. Gosling, J., McComas, D., Roberts, D. & Skoug, R. A one-sided aspect of Alfvénic fluctuations in the solar wind. *Astrophys. J.* **695**, 213 (2009).
7. Matteini, L., Horbury, T. S., Neugebauer, M. & Goldstein, B. E. Dependence of solar wind speed on the local magnetic field orientation: role of Alfvénic fluctuations. *Geophys. Res. Lett.* **41**, 259–265 (2014).
8. Hou, C. et al. Nature, generation, and dissipation of Alfvénic kinks/switchbacks observed by Parker Solar Probe and wind. *Astrophys. J.* **950**, 157 (2023).
9. Shoda, M., Yokoyama, T. & Suzuki, T. K. A self-consistent model of the coronal heating and solar wind acceleration including compressible and incompressible heating processes. *Astrophys. J.* **853**, 190 (2018).
10. Verscharen, D., Bale, S. D. & Velli, M. Flux conservation, radial scalings, mach numbers, and critical distances in the solar wind: magnetohydrodynamics and Ulysses observations. *Mon. Not. R. Astron. Soc.* **506**, 4993–5004 (2021).
11. Squire, J., Chandran, B. D. & Meyrand, R. In-situ switchback formation in the expanding solar wind. *Astrophys. J. Lett.* **891**, 2 (2020).
12. Zank, G., Nakanotani, M., Zhao, L.-L., Adhikari, L. & Kasper, J. The origin of switchbacks in the solar corona: linear theory. *Astrophys. J.* **903**, 1 (2020).
13. He, J. et al. Solar origin of compressive Alfvénic spikes/kinks as observed by Parker Solar Probe. *Astrophys. J. Lett.* **913**, 14 (2021).
14. Shoda, M., Chandran, B. D. & Cranmer, S. R. Turbulent generation of magnetic switchbacks in the Alfvénic solar wind. *Astrophys. J.* **915**, 52 (2021).
15. Drake, J. et al. Switchbacks as signatures of magnetic flux ropes generated by interchange reconnection in the corona. *Astron. Astrophys.* **650**, 2 (2021).
16. Tenerani, A. et al. Magnetic field kinks and folds in the solar wind. *Astrophys. J. Suppl. Ser.* **246**, 32 (2020).
17. Schwadron, N. & McComas, D. Switchbacks explained: super-Parker fields-the other side of the sub-Parker spiral. *Astrophys. J.* **909**, 95 (2021).
18. Ruffolo, D. et al. Shear-driven transition to isotropically turbulent solar wind outside the Alfvén critical zone. *Astrophys. J.* **902**, 94 (2020).
19. Fargette, N. et al. Characteristic scales of magnetic switchback patches near the Sun and their possible association with solar supergranulation and granulation. *Astrophys. J.* **919**, 96 (2021).
20. Tian, H., Marsch, E., Tu, C.-Y., Xia, L.-D. & He, J.-S. Sizes of transition-region structures in coronal holes and in the quiet Sun. *Astron. Astrophys.* **482**, 267–272 (2008).
21. Shen, Y. Observation and modelling of solar jets. *Proc. R. Soc. A* **477**, 20200217 (2021).
22. Shibata, K. et al. Observations of X-ray jets with the Yohkoh soft X-ray telescope. *Publ. Astron. Soc. Jpn* **44**, 173–179 (1992).
23. Pariat, E., Antiochos, S. & DeVore, C. A model for solar polar jets. *Astrophys. J.* **691**, 61 (2009).
24. Chen, Y. et al. Imaging a magnetic-breakout solar eruption. *Astrophys. J. Lett.* **820**, 37 (2016).
25. Sterling, A. C., Moore, R. L. & Panesar, N. K. Magnetic flux cancelation as the buildup and trigger mechanism for cme-producing eruptions in two small active regions. *Astrophys. J.* **864**, 68 (2018).
26. Panesar, N. K., Sterling, A. C., Moore, R. L. & Chakrapani, P. Magnetic flux cancelation as the trigger of solar quiet-region coronal jets. *Astrophys. J. Lett.* **832**, 7 (2016).
27. Panesar, N. K., Sterling, A. C. & Moore, R. L. Magnetic flux cancelation as the trigger of solar coronal jets in coronal holes. *Astrophys. J.* **853**, 189 (2018).
28. Wyper, P. F., Antiochos, S. K. & DeVore, C. R. A universal model for solar eruptions. *Nature* **544**, 452–455 (2017).
29. Sterling, A. C. & Moore, R. L. Coronal-jet-producing minifilament eruptions as a possible source of Parker Solar Probe switchbacks. *Astrophys. J. Lett.* **896**, 18 (2020).
30. Sterling, A. C., Moore, R. L., Panesar, N. K. & Samanta, T. Possible evolution of minifilament-eruption-produced solar coronal jets, jetlets, and spicules, into magnetic-twist-wave "switchbacks" observed by the Parker Solar Probe (PSP). *J. Phys. Conf. Ser.* **1620**, 012020 (2020).
31. Moore, R. L., Tiwari, S. K., Panesar, N. K. & Sterling, A. C. Prospective implications of extreme-ultraviolet coronal plumes for magnetic-network genesis of coronal heating, coronal-hole solar wind, and solar-wind magnetic field switchbacks. *Astrophys. J. Lett.* **945**, 16 (2023).
32. Yang, L. et al. Excitation of magnetohydrodynamic waves by plasmoids ejection in the solar corona. *AIP Conf. Proc.* **1720**, 040022 (2016).
33. Rouillard, A. P. et al. Relating streamer flows to density and magnetic structures at the Parker Solar Probe. *Astrophys. J. Suppl. Ser.* **246**, 37 (2020).
34. Griton, L. et al. Coronal bright points as possible sources of density variations in the solar corona. *Astrophys. J.* **893**, 64 (2020).
35. Pesnell, W. D., Thompson, B. J. & Chamberlin, P. C. The Solar Dynamics Observatory (SDO). *Sol. Phys.* **275**, 3–15 (2012).
36. Tian, H. et al. Prevalence of small-scale jets from the networks of the solar transition region and chromosphere. *Science* **346**, 1255711 (2014).
37. Gary, G. A. Linear force-free magnetic fields for solar extrapolation and interpretation. *Astrophys. J. Suppl. Ser.* **69**, 323–348 (1989).
38. Sterling, A. C. et al. Inconspicuous solar polar coronal X-ray jets as the source of conspicuous Hinode/EUV imaging spectrometer Doppler outflows. *Astrophys. J.* **940**, 85 (2022).
39. Raouafi, N.-E. & Stenborg, G. Role of transients in the sustainability of solar coronal plumes. *Astrophys. J.* **787**, 118 (2014).
40. Panesar, N. K. et al. IRIS and SDO observations of solar jetlets resulting from network-edge flux cancelation. *Astrophys. J. Lett.* **868**, 27 (2018).
41. Panesar, N. K. et al. Hi-C 2.1 observations of jetlet-like events at edges of solar magnetic network lanes. *Astrophys. J. Lett.* **887**, 8 (2019).
42. Berghmans, D. et al. Extreme-UV quiet sun brightenings observed by the Solar Orbiter/EUI. *Astron. Astrophys.* **656**, 4 (2021).
43. Panesar, N. K. et al. The magnetic origin of solar campfires. *Astrophys. J. Lett.* **921**, 20 (2021).
44. Huang, Z. et al. Heating at the remote footpoints as a brake on jet flows along loops in the solar atmosphere. *Astrophys. J.* **897**, 113 (2020).
45. Madjarska, M. S., Mackay, D. H., Galsgaard, K., Wiegelmann, T. & Xie, H. Eruptions from coronal bright points: a spectroscopic view by IRIS of a mini-filament eruption, QSL reconnection, and reconnection-driven outflows. *Astron. Astrophys.* **660**, 45 (2022).

46. Suzuki, T. K. & Inutsuka, S.-i Making the corona and the fast solar wind: a self-consistent simulation for the low-frequency Alfvén waves from the photosphere to 0.3 au. *Astrophys. J.* **632**, 49 (2005).

47. Matsumoto, T. & Suzuki, T. K. Connecting the sun and the solar wind: The first 2.5-dimensional self-consistent MHD simulation under the Alfvén wave scenario. *Astrophys. J.* **749**, 8 (2012).

48. Cranmer, S. & Van Ballegooijen, A. On the generation, propagation, and reflection of Alfvén waves from the solar photosphere to the distant heliosphere. *Astrophys. J. Suppl. Ser.* **156**, 265 (2005).

49. Verdini, A. & Velli, M. Alfvén waves and turbulence in the solar atmosphere and solar wind. *Astrophys. J.* **662**, 669 (2007).

50. Mozer, F. S. et al. On the origin of switchbacks observed in the solar wind. *Astrophys. J.* **919**, 60 (2021).

51. Roberts, M. A., Uritsky, V. M., DeVore, C. R. & Karpen, J. T. Simulated encounters of the Parker Solar Probe with a coronal-hole jet. *Astrophys. J.* **866**, 14 (2018).

52. Telloni, D. et al. Observation of a magnetic switchback in the solar corona. *Astrophys. J. Lett.* **936**, 25 (2022).

53. Macneil, A. R., Owens, M. J., Finley, A. J. & Matt, S. P. A statistical evaluation of ballistic backmapping for the slow solar wind: the interplay of solar wind acceleration and corotation. *Mon. Not. R. Astron. Soc.* **509**, 2390–2403 (2022).

54. Altschuler, M. D. & Newkirk, G. Magnetic fields and the structure of the solar corona. *Sol. Phys.* **9**, 131–149 (1969).

55. Stansby, D., Yeates, A. & Badman, S. T. pfsspy: a Python package for potential field source surface modelling. *J. Open Source Softw.* **5**, 2732 (2020).

56. Bale, S. et al. The fields instrument suite for Solar Probe Plus. *Space Sci. Rev.* **204**, 49–82 (2016).

57. Lee, C. et al. Coronal field opens at lower height during the solar cycles 22 and 23 minimum periods: IMF comparison suggests the source surface should be lowered. *Sol. Phys.* **269**, 367–388 (2011).

58. Moses, J. D. et al. Global helium abundance measurements in the solar corona. *Nat. Astron.* **4**, 1134–1139 (2020).

59. Kasper, J. C., Stevens, M. L., Lazarus, A. J., Steinberg, J. T. & Ogilvie, K. W. Solar wind helium abundance as a function of speed and heliographic latitude: variation through a solar cycle. *Astrophys. J.* **660**, 901 (2007).

60. Kasper, J. et al. Evolution of the relationships between helium abundance, minor ion charge state, and solar wind speed over the solar cycle. *Astrophys. J.* **745**, 162 (2012).

61. Fisk, L., Schwadron, N. & Zurbuchen, T. On the slow solar wind. *Space Sci. Rev.* **86**, 51–60 (1998).

62. Parker, E. N. Dynamics of the interplanetary gas and magnetic fields. *Astrophys. J.* **128**, 664 (1958).

63. Kasper, J. C. et al. Solar Wind Electrons Alphas and Protons (SWEAP) investigation: design of the solar wind and coronal plasma instrument suite for Solar Probe Plus. *Space Sci. Rev.* **204**, 131–186 (2016).

64. Mozer, F. et al. Switchbacks in the solar magnetic field: their evolution, their content, and their effects on the plasma. *Astrophys. J. Suppl. Ser.* **246**, 68 (2020).

65. Kasper, J. et al. Parker Solar Probe enters the magnetically dominated solar corona. *Phys. Rev. Lett.* **127**, 255101 (2021).

66. Lemen, J. R. et al. The Atmospheric Imaging Assembly (AIA) on the Solar Dynamics Observatory (SDO). *Sol. Phys.* **275**, 17–40 (2012).

67. Scherrer, P. H. et al. The Helioseismic and Magnetic Imager (HMI) investigation for the Solar Dynamics Observatory (SDO). *Sol. Phys.* **275**, 207–227 (2012).

68. The SunPy Community et al. The SunPy project: open source development and status of the version 1.0 core package. *Astrophys. J.* **890**, 68 (2020).

69. Müller, D. et al. JHelioviewer: time-dependent 3D visualisation of solar and heliospheric data. *Astron. Astrophys.* **606**, 10 (2017).

70. Riley, P. et al. A multi-observatory inter-comparison of line-of-sight synoptic solar magnetograms. *Sol. Phys.* **289**, 769–792 (2014).

71. Ramachandran, P. & Varoquaux, G. Mayavi: 3D visualization of scientific data. *Comput. Sci. Eng.* **13**, 40–51 (2011).

Acknowledgements

Author contributions

Competing interests

Additional information